Dalton Transactions

ROYAL SOCIETY OF CHEMISTRY

PAPER

View Article Online
View Journal

Cite this: DOI: 10.1039/d6dt00235h

DNA-interacting lanthanide complexes with a DOTA-derived dipyrido[3,2-*a*;2′,3′-*c*]phenazine ligand for near-infrared luminescence

Marek Beliš, *[a] Jakub Šrein,[b] Subhrajyoti Bhandary, [a] Simona Premcheska,[c] Mirijam Lederer,[c] Ian Pompermayer Machado, [c] Anna M. Kaczmarek [c] and Kristof Van Hecke *[a]

Dipyrido[3,2-*a*:2′,3′-*c*]phenazine (dppz) is well known for its ability to interact with DNA and is ideally suited for sensitizing near-infrared (NIR)-emitting lanthanide ions such as Nd^{3+}, Er^{3+} and Yb^{3+}. The combination of these properties gives perspective for the utilization of lanthanide complexes incorporating a dppz moiety for biomedical applications. Here, we present the synthesis of novel lanthanide complexes with an embedded dppz moiety [Ln(DO3A-dppz)] (Ln = all lanthanides except Pm; DO3A = 1,4,7,10-tetraazadodecane-1,4,7-triacetic acid) derived from clinically used [Ln(DOTA)] complexes (DOTA = 1,4,7,10-tetraazadodecane-1,4,7,10-tetraacetic acid). Structural analyses of all the complexes reveal interesting behavior, showing a share of isomers in the structures linked to lanthanide contraction and ionic radii. Photoluminescence studies provide excitation and emission spectra of the complexes with compatible central ions Nd^{3+}, Er^{3+}, Yb^{3+} and Eu^{3+}, along with decay times of the complexes with Yb^{3+} and Eu^{3+}. All complexes are weakly soluble in water with good stability in Tris-HCl buffer, and their affinity towards model calf-thymus DNA was tested using a SYBR Green I displacement assay. Overall, the obtained results are promising for the development of [Ln(DO3A-dppz)] complexes towards future applications in biomedical imaging.

Received 29th January 2026,
Accepted 11th May 2026

DOI: 10.1039/d6dt00235h

rsc.li/dalton

1 Introduction

Lanthanide chemistry is a dynamic field undergoing continuous development. The distinctive structural, optical, and magnetic attributes exhibited by lanthanide complexes make them versatile tools in multiple applications, especially in the fields of biology and medicine.[1,2] These complexes are currently in practical use or demonstrate substantial potential across diverse roles, including serving as MRI contrast agents (notably Gd^{3+} compounds),[3,4] fluorescent probes,[5,6] bioresponsive cellular imaging agents,[7] and artificial nucleases proficient in cleaving RNA or DNA.[8] Recent investigations focus on the capabilities of other lanthanide compounds, such as oxide nanoparticles (*e.g.* CeO_2),[9] nanodrums,[10] nanocrystals or radioisotopes (*e.g.*, ^{177}Lu),[11] acting as agents in biomedical imaging and cancer therapy. The prevalent +3 oxidation state characterizing lanthanides is important in these applications, ensuring redox stability crucial for cellular applications, particularly in hypoxic cancer cells.[1]

Many of the applications are based on the unique luminescence properties of lanthanides, which are emitted from the UV-visible (UV-Vis) to near-infrared (NIR) region with relatively long luminescence lifetimes.[12–14] In the context of biological applications, luminescent materials emitting in the NIR spectrum within the biological windows (between 650–950 nm, 1000–1350 nm and 1500–1800 nm) present distinct advantages over their visible-emitting counterparts.[15] Within these biological windows, NIR-emitting materials are less damaging to biological tissues and provide better optical imaging resolution, as the scattering and absorption of light by tissues, blood and water are minimal. This makes imaging of deeper-seated tumor cells more feasible compared to visible or UV light.[16] Lanthanide ions demonstrating NIR emission under suitable conditions are Pr^{3+}, Nd^{3+}, Sm^{3+}, Dy^{3+}, Ho^{3+}, Er^{3+}, Tm^{3+} and Yb^{3+}, with Nd^{3+}, Er^{3+} and Yb^{3+} in particular emphasis being frequently investigated. However, lanthanide f–f transitions are partially forbidden by the parity rule, leading to low absorption coefficients, which is a significant hindrance in full utilization of their luminescence properties. As a result, high-power

[a]*XStruct, Department of Chemistry, Ghent University, Krijgslaan 289-S3, B-9000 Ghent, Belgium. E-mail: Marek.Belis@UGent.be, Kristof.VanHecke@UGent.be*
[b]*Department of Inorganic Chemistry, Charles University, Hlavova 2030, Prague, 182 00, Czech Republic*
[c]*NanoSensing, Department of Chemistry, Ghent University, Krijgslaan 289-S3, B-9000 Ghent, Belgium*

sources (*e.g.* lasers) are necessary for excitation to reach higher emission intensities. Mitigation of this drawback can be achieved through the strategic design of lanthanide complexes with organic ligands containing strongly absorbing chromophores.[12,13]

Selection of an appropriate organic ligand is of significant importance in the design of lanthanide complexes with desired functions. Considerable efforts have been dedicated to the challenge of obtaining highly emissive lanthanide complexes in the NIR region, which would combine multiple aspects for feasible applications.[17–19] Our focus lies in the strategic design of lanthanide complexes incorporating dipyrido[3,2-*a*:2′,3′-*c*]phenazine (dppz, Fig. 1), as its triplet energy level is optimally suited for efficient sensitization of Nd^{3+}, Er^{3+} and Yb^{3+}, and also Eu^{3+} ions.[20,21]

For instance, a previously reported [$Er(Hbta)_3$(dppz)] complex (Hbta = benzoyltrifluoroacetone) demonstrated increased NIR emission compared to analogous complexes synthesized with the Hbta ligand in combination with bipyridine, phenanthroline, or dipyrido[3,2-*d*:2′,3′-*f*]quinoxaline (dpq).[24] Multiple investigations report complexes with potential in biological applications containing dpq and dppz also with other co-ligands, including chloride anions with water, nitrate anions, or tolfenamic acid.[25–28] Advancements include the synthesis of an [$Yb(L)_3$dppz] complex (L = 3,5-heptanedione), exhibiting strong NIR luminescence. Such complexes were incorporated into poly (methyl methacrylate) (PMMA) thin films, with potential applications explored in the biological field.[29] Ytterbium(III) complexes, such as [Yb(dppz)$(DMF)_2Cl_3$] and [Yb(dppz)$(ttfa)_3$] (Httfa = 4,4,4-trifluoro-1-(2-thienyl)-1,3-butanedione), were purposefully designed as NIR bioimaging probes, showing cooperative upconversion luminescence for theranostic applications within the biological phototherapeutic window.[30]

Polypyridyl ligands such as dppz have the intrinsic capability to interact with DNA tracts, providing advantages in applications over other suitable chromophores.[31–33] This characteristic makes them ideal candidates for incorporation in NIR luminescent probes for cellular imaging and diagnostics, particularly when coupled with specific lanthanides. Many transition metal complexes with dppz have been shown to intercalate into DNA sequences,[34–39] but this type of interaction has barely been explored for lanthanides.[21] In addition, the reported compounds are usually not soluble in water or other biocompatible solvents, which hampers their effective use in biomedical applications. As a first step toward evaluating the intercalation potential of lanthanide complexes, we have developed water-soluble lanthanide complexes containing a single dppz moiety, taking inspiration from clinically used MRI contrast agents such as [Gd(DOTA)] (Fig. 1), as well as related molecules reported by Poole *et al.*[22] Very recently, two water-soluble luminescent macrocyclic Eu(III) probes were reported to be able to selectively recognize physiological phosphates,[23] while macrocyclic luminescent Tb(III) probes containing amino acid-based antennae were reported to be able to discriminate between adenine and guanine nucleotides.[40] In this work, we present the non-trivial multistep synthesis of a novel nonadentate ligand DO3A-dppz (L), along with all feasible lanthanide complexes of this ligand [Ln·L] (Ln = whole lanthanide series except Pm). The formation of all complexes was confirmed by HRMS, and their structures were characterized by single-crystal X-ray diffraction (SCXRD) analysis, revealing interesting coordination behavior consistent with lanthanide contraction. Furthermore, we report a detailed luminescence study of the NIR-emitting complexes [Nd·L], [Er·L] and [Yb·L], as well as visible-emitting [Eu·L]. The stability of the complexes was evaluated by UV-Vis spectroscopy, and the interaction potential with DNA was tested by a fluorescence study using the [Nd·L] complex and calf-thymus DNA (CT-DNA) as a model.

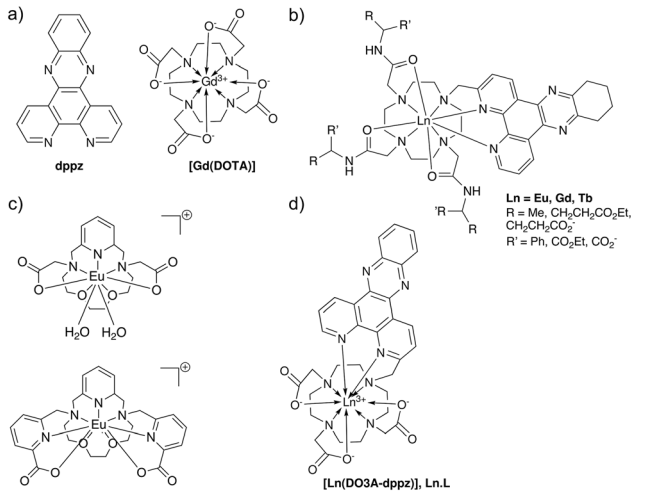

Fig. 1 (a) Dipyrido[3,2-*a*:2′,3′-*c*]phenazine (dppz) and the clinically used MRI contrast agent, [Gd(DOTA)] complex (DOTA = 1,4,7,10-tetraazadodecane-1,4,7,10-tetraacetic acid). (b) Related macrocyclic cyclene-based luminescent Ln(III) probes, with tetraazatriphenylene chromophores.[22] (c) Very recently reported luminescent macrocyclic Eu(III) probes for selective recognition of physiological phosphates.[23] (d) This work, reporting the novel nonadentate ligand DO3A-ddpz (L), along with all its feasible lanthanide complexes [Ln·L] (Ln = whole lanthanide series except Pm).

2 Results and discussion

Synthetic modifications of polypyridyl ligands are generally challenging, due to the limited solubility of various intermediates or the final compounds. Another obstacle lies in controlling the site of the intended modification, which – together with the separation of various byproducts – makes these synthetic steps particularly demanding. Nevertheless, we have managed to adapt and optimize procedures reported for similar molecules,[21,22,41] enabling the full characterization of several new intermediates leading to the final complexes (Scheme 1). Key steps in this synthesis route are the preparation of Me-phen, O=Me-dppz and Br-Me-dppz.

The first step in our synthetic route involved the introduction of a methyl group in the correct position on 1,10-phenanthroline, achieved *via* a two-step reaction with methyllithium

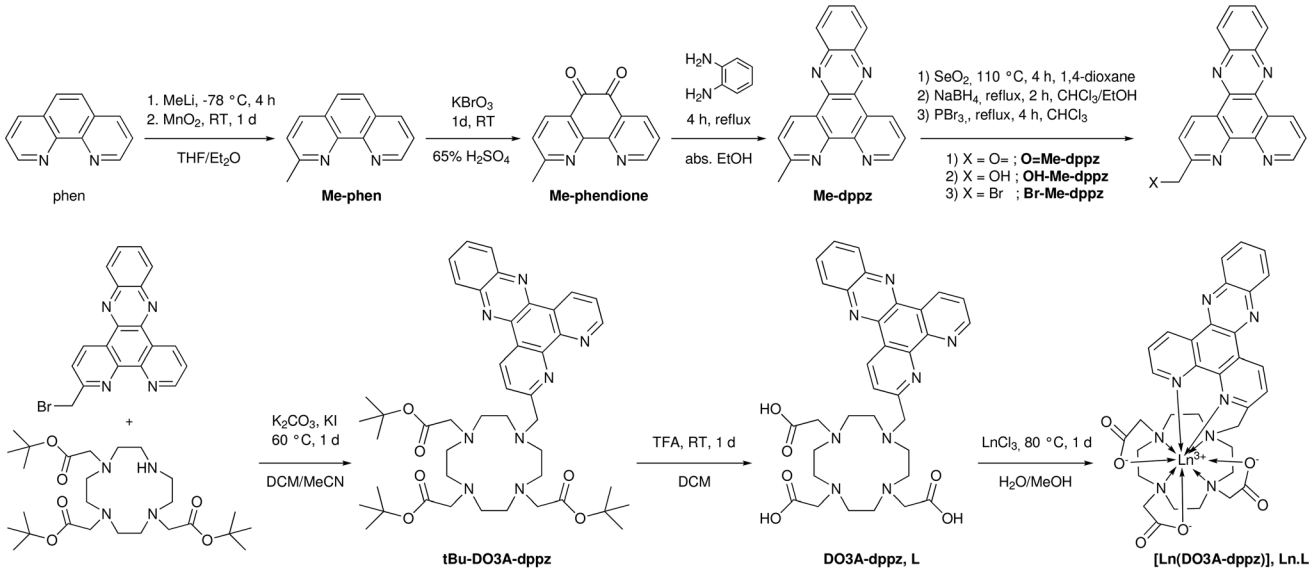

Scheme 1 Synthesis of [Ln(DO3A-dppz)], [Ln·L] complexes (Ln = all lanthanides except Pm, DO3A = 1,4,7,10-tetraazadodecane-1,4,7-triacetic acid, and dppz = dipyrido[3,2-*a*:2′,3′-*c*]phenazine).

and subsequently MnO_2.[22,41] Cooling the reaction mixture in the first step to −78 °C using dry ice significantly increased the yield to more than 80%, compared to about 20% achieved at 0 °C. Moreover, with a high share of the desired product in the reaction mixture, crystallization directly from the final filtrate was observed. SCXRD analysis of the resulting crystals revealed a previously unreported solvate of Me-phen, incorporating water molecules into the structure. Presumably, residual solvent moisture or environmental humidity is sufficient to induce growth of the crystals with stabilization by hydrogen bonds (Fig. 2a). In fact, this approach provides a simple way of isolating pure Me-phen without the necessity for chromatography, easily separating minor amounts of unreacted phenanthroline or the double-methylated derivative. If the separation of byproducts has been performed properly with Me-phen, recrystallization of the crude Me-phendione solid yields a clean product. Additionally, Me-dppz is more soluble than its unmodified counterpart dppz, reducing the yield and efficiency of collecting the product by recrystallization. Nevertheless, this stage represents the last opportunity to reliably control the output before the purity can be anchored again with the formation of Br-Me-dppz.

A stepwise redox approach was selected instead of direct halogenation of the methyl group, considering the risk of preferential halogenation of other positions.[22,42] The synthesis of O═Me-dppz requires careful attention due to the relative ease of overoxidation by SeO_2 to the corresponding carboxylic acid. Excess SeO_2, or significant amounts of unfiltered Se salts and other precipitates from the reaction, can render future processing impossible, especially after the following reduction with $NaBH_4$. Where overoxidized products or other solid materials are present, the reduction reaction yields an insoluble amorphous purple material. All these complications also hamper effective purification of these intermediates, which makes the use of crude materials more reasonable. However, when these steps are performed correctly, the exchange of a hydroxy group for a halogen does not pose a significant problem. With increased solubility of Br-Me-dppz, the remaining salts and byproducts from the previous reactions, including unreacted Me-dppz, can be effectively removed at this stage using either silica gel or reverse-phase chromatography. The purity of the resulting material also provides an opportunity for crystallization, facilitating structural confirmation by SCXRD (Fig. 2b).

Following alkylation of *t*Bu-DO3A, deprotection of the acetates using trifluoroacetic acid (TFA) proceeded as expected, consistent with the multiple usages of these reactions. The structure of *t*Bu-DO3A-dppz could even be determined (Fig. S1). However, neither the final ligand nor the complexes

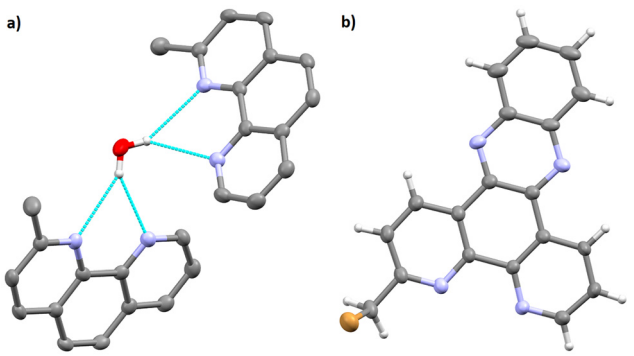

Fig. 2 (a) Potential O–H···N hydrogen bonds between a water molecule and Me-phen. Hydrogen atoms of Me-phen are omitted for clarity. (b) Molecular structure of Br-Me-dppz. The DCM solvate molecule is omitted.

[Ln·L] could be purified using ionic exchangers, probably due to the interaction between the dppz moiety and the active groups of the exchanger. As such, the ligand was used directly after deprotection, without additional purification, for complexation. The final reverse-phase chromatography was performed without the addition of TFA, avoiding the presence of salts in the freeze-dried material of the complexes [Ln·L]. Formation of the complexes was confirmed by HRMS, and crystal structures of all complexes were obtained by recrystallization from MeOH.

SCXRD analysis shows that the complexes crystallize in the centrosymmetric monoclinic space groups $P2_1/c$ or $P2_1/n$. The length of the a axis varies in a narrow interval from 8.5586(2) Å to 8.6137(2) Å, whereas the c axis shows a larger variation between 27.3149(3) Å and 29.2955(7) Å, with the general trend of decreasing with smaller Ln ionic radii. In contrast, a clear trend can be observed for the b axis, increasing in length from 16.3922(3) Å for La to 16.6043(3) Å for Lu.

As an example, the crystal structure of [Nd·L] will be discussed. The structure of [Nd·L] (Fig. 3) shows a nonadentate coordination of the ligand in a typical capped twisted-square-antiprismatic (TSA) environment. One of the dppz nitrogens, N(8), completes the coordination plane formed by the acetate oxygens, while another nitrogen, N(7), occupies the capping position. To allow such coordination, the position of the central atom is slightly eccentric relative to the DOTA-like cage. Simultaneously, the rigid aromatic structure of the dppz moiety adapts through bending of the pyridyl rings out of the phenazine plane, with dihedral angles of 7.5° for the pyridyl ring containing N(7) and 8.2° for the pyridyl ring containing N(8). Bond distances between Nd(1) and the cyclene nitrogens are 2.718(3), 2.729(3), 2.686(3) and 2.652(3) Å for Nd(1)–N(1–4), respectively. The bond distances to atoms in the acetate plane (defined by coordinating oxygens and N(8)) are 2.409(3), 2.388 (2) and 2.400(2) Å for Nd(1)–O(1,3,5), respectively, with a Nd (1)–N(8) bond distance of 2.609(2) Å. The final coordination bond distance for Nd(1)–N(7) is 2.681(3) Å, completing the coordination environment.

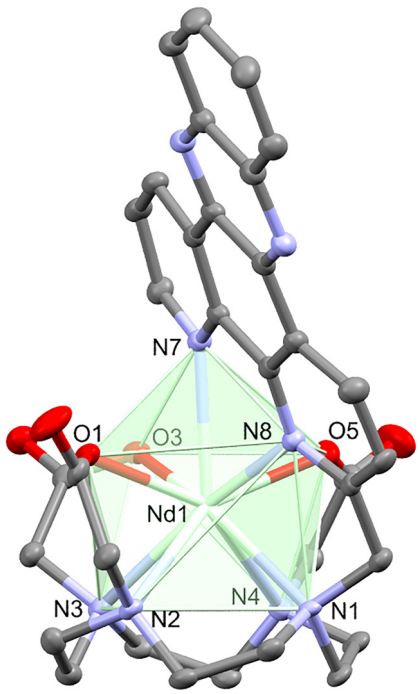

Fig. 3 Coordination environment of [Nd·L] exhibiting nonadentate coordination in a capped twisted-square-antiprismatic (TSA) isomer. Hydrogen atoms are omitted for clarity.

These values vary across the lanthanide series, with dihedral angles of the pyridyl planes in the [La·L] complex being 6.3° and 8.0° and increasing to 8.8° and 9.9° in the case of [Lu·L]. The bond distances follow the general trend according to typical lanthanide contraction. For example, in [La·L], the La(1)–N(1–4) distances are 2.767(3), 2.800(3), 2.736(4) and 2.711(4) Å, respectively. The La(1)–O(1,3,5) distances are 2.460 (3), 2.435(3) and 2.460(3) Å, respectively, with a La(1)–N(8) bond of 2.661(4) Å and a La(1)–N(7) bond of 2.710(4) Å. In the case of [Lu·L], the Lu(1)–N(1–4) bond distances are 2.635(7), 2.726(7), 2.627(8) and 2.581(6) Å, respectively, and the Lu(1)–O (1,3,5) distances are 2.289(3), 2.234(2) and 2.248(2) Å, respectively, with additional bonds of 2.463(3) Å for Lu(1)–N(8) and 2.609(3) Å for Lu(1)–N(7) (Table S2). All lanthanide complexes adopt a nonadentate coordination; however, the preferred coordination number of the late lanthanides is 8. To compensate for this coordination number and the lanthanide contraction, both square-antiprismatic (SA) and TSA isomers are observed in the crystal structures of the [Ho·L] to [Lu·L] complexes (Fig. 4 and Fig. S3 and S4) in the form of both ring conformations,[43] whereas only the TSA isomer is observed up to Dy. Moreover, the share of the SA isomer increases with decreasing ionic radii, reaching 45% in the Lu complex. Therefore, the trend in Ln–N(1–4) bond distances is less clear, with similar values across the [Ho·L] to [Lu·L] structures for both TSA and SA conformations. However, for the coordinating atoms in the acetate plane, the decreasing trend for the Ln(1)–O(1,3,5) and Ln(1)–N(8) bond distances is still clear, with a highest Ho(1)–O(1) distance of 2.332(3) Å and a lowest Lu(1)–O (3) distance of 2.234(2) Å, while the Ho(1)–N(8) distance of 2.514(3) Å decreases gradually towards a Lu(1)–N(8) distance of 2.463(3) Å (Table S2).

Interestingly, not all single crystals exhibited the same behavior while being manipulated for SCXRD data collection. Although all crystals looked similar under their crystallization conditions, those of the complexes from La up to Tb remained stable when manipulated in Paratone® N oil. In contrast, only a small fraction of crystals of the complexes from Dy to Lu retained their single crystallinity in the oil, while the majority of these crystals lost their integrity within a few minutes. We hypothesize that the relative share of the SA isomer in the crystals determines their resilience towards migration of oil or residual methanol through the solvent channels in the respective structures (Fig. S5 and S6), hence increasing the durability of the single-crystalline phase outside of the crystallization conditions.

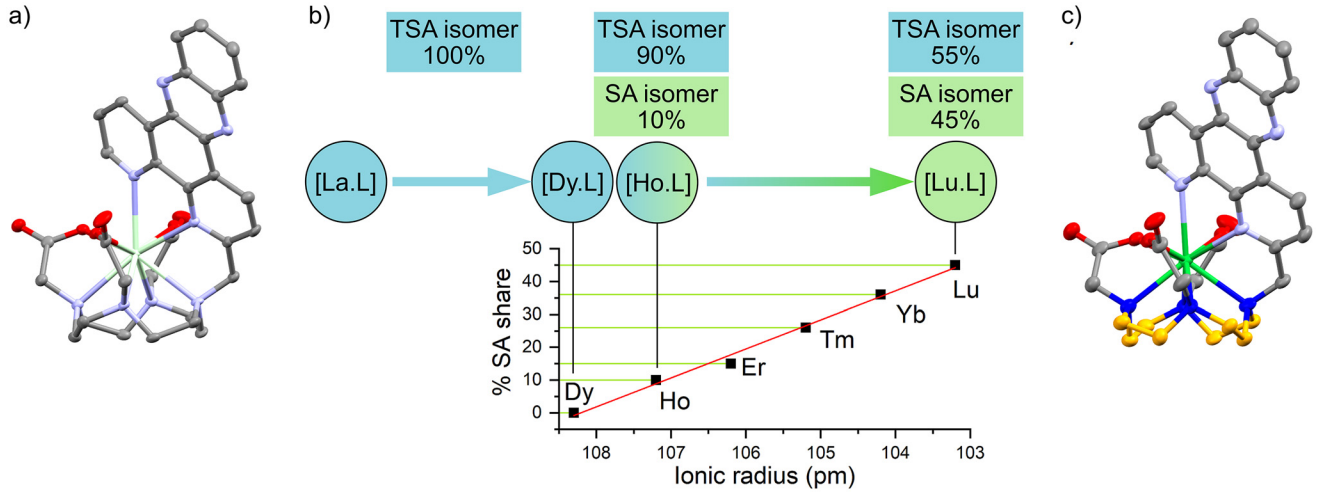

Fig. 4 (a) Molecular structure of [Nd·L], composed purely of the TSA isomer. (b) Schematic representation of isomer development throughout the Ln series. Up to [Dy·L], only the TSA isomer is present, while from [Ho·L] to [Lu·L], the share of the SA isomer increases towards 45%. (c) SA isomer of the [Yb·L] complex, with the new conformation of the cyclene ring emphasized in orange and dark blue. In all cases, hydrogen atoms are omitted for clarity.

A photoluminescence study of the obtained solid complexes provides the excitation and emission spectra of [Nd·L], [Er·L], [Yb·L] and [Eu·L] (Fig. 5 and 6, respectively), as these central ions are compatible with efficient sensitization by dppz due to their low accepting levels. The photoluminescence of the complexes in an aqueous solution was also recorded (Fig. S7). The results are in accordance with previously reported Ln-dppz complexes.[21] In all cases, the excitation spectra display a broad band extending from approximately 260 nm to 430 nm, with a maximum at around 396 nm (399, 393 and 396 nm for [Nd·L], [Er·L] and [Yb·L], respectively). Emission of the complexes was observed at RT after excitation at 390 nm. In the case of [Nd·L], three distinctive peaks are visible with maxima at 879 nm ($^4F_{3/2} \rightarrow {}^4I_{9/2}$), 1056 nm ($^4F_{3/2} \rightarrow {}^4I_{11/2}$) and 1330 nm ($^4F_{3/2} \rightarrow {}^4I_{13/2}$). The [Er·L] complex shows a characteristic NIR peak in the range of 1400–1650 nm, with a maximum at 1535 nm ($^4I_{13/2} \rightarrow {}^4I_{15/2}$), whereas the [Yb·L] spectrum shows an emission peak in the range of 850–1060 nm, with a maximum at 979 nm ($^2F_{5/2} \rightarrow {}^2F_{7/2}$).

The excitation and emission spectra of the [Eu·L] complex are presented in Fig. 6. The Eu^{3+} ion is known as a powerful spectroscopic probe, providing additional insight into the complexes' coordination environment. In the excitation spectrum, the broad excitation band originating from the dppz ligand ranges from 300 to 450 nm, but it shows a remarkably high intensity in the 380–430 nm range. This indicates a superior dppz → Ln^{3+} energy-transfer efficiency when Ln = Eu compared to the other lanthanide complexes, likely due to a closer energetic match between the dppz-donating levels and the Eu^{3+}-accepting levels. The energy-transfer pathways in these complexes will be discussed in more detail later. In the emission spectra, all Eu^{3+} emissions arising from the lowest excited energy level $^5D_0 \rightarrow {}^7F_{0-4}$ transitions were assigned. The Eu^{3+} ion is inserted into a nonadentate coordination site, similar to that of Nd^{3+} (Fig. 3), *i.e.*, a capped twisted-square-antiprismatic (TSA) site with C_{4v} symmetry. In this symmetry, the hypersensitive $^5D_0 \rightarrow {}^7F_2$ transition is expected to show a maximum of three Stark splitting bands, since the $^5D_0$ level is

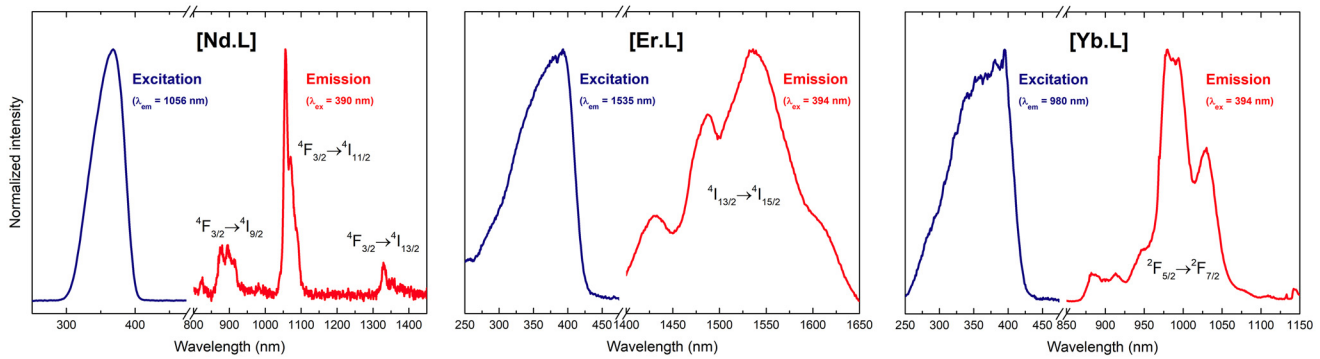

Fig. 5 Combined excitation and emission spectra of [Nd·L], [Er·L] and [Yb·L] complexes. Emission spectra were recorded after excitation at 390 nm.

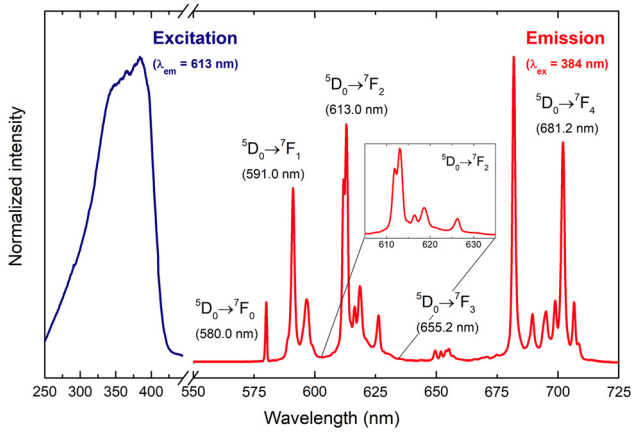

Fig. 6 Combined excitation (blue) and emission (red) spectra of [Eu·L] recorded using the sample in powder form. The emission spectrum was recorded with a step size of 0.2 nm and the $^5D_0 \rightarrow {}^7F_{0-4}$ transitions of Eu^{3+} were assigned, showing the wavelength corresponding to the highest intensity for each transition. The inset shows a zoom of the $^5D_0 \rightarrow {}^7F_2$ transition.

non-degenerate.[44] However, five peaks are clearly visible (inset in Fig. 6). The first hypothesis raised was that Eu^{3+} was inserted in two (or more) sites with different symmetries. Nonetheless, this does not seem to be the case, as the $^5D_0 \rightarrow {}^7F_0$ transition appears as a very sharp, single peak with no distortions or shoulders, indicating the presence of a single symmetry site. This is expected since the TSA → SA isomer transition occurs only for complexes of heavier lanthanide ions (from Dy to Lu). Therefore, the most plausible explanation is that Eu^{3+} experiences microsymmetry distortions[45] of the C_{4v} site. The bond distances observed for the Nd^{3+} complex vary significantly from 2.388 Å [Nd(1)–O(3)] to 2.729 Å [Nd(1)–N(2)], corresponding to a variation of 12.5% in bond length due to the different donor atoms (N and O) coordinated to Nd^{3+}. The dihedral angles also vary when decreasing the Ln^{3+} radius along the La–Lu series. Therefore, the additional Stark splitting observed in the Eu^{3+} emission is a consequence of the strongly distorted TSA site, which deviates from perfect C_{4v} symmetry. Interestingly, the comparable intensities between the magnetic dipole-allowed $^5D_0 \rightarrow {}^7F_1$ transition and the hypersensitive $^5D_0 \rightarrow {}^7F_2$ transition indicate that the site distortion does not significantly reduce the local symmetry (*e.g.*, $C_{4v} \rightarrow C_1$). Otherwise, the $^5D_0 \rightarrow {}^7F_2$ emission would be relatively much more intense. Similar $^5D_0 \rightarrow {}^7F_0/{}^5D_0 \rightarrow {}^7F_2$ intensity ratios were found for analogous SSS-Δ and RRR-Δ $EuPh_3DPQ$ complexes, which also possess nonadentate-capped TSA sites,[22] although no direct band-splitting comparison can be made since those are enantiomeric compounds.

Luminescence decay times were subsequently measured. While the results for [Nd·L] and [Er·L] are not considered reliable due to the expected short lifetimes and limitations of the used electronics, [Yb·L] provides an acceptable result (Fig. S8). The decay curve was well fitted with a monoexponential function, indicating the presence of a single emissive entity in the sample, and the decay time was determined to be 5.0 μs. This hypothesis is corroborated by the non-convergence of biexponential fitting to the same data points. To further explore this hypothesis, photoluminescence decay curves of the [Eu·L] complex were measured in both the solid state (single crystal) and an aqueous solution (Fig. S9). After excluding the first data points (0–0.2 ms) that correspond to the instrument response function (IRF) dominated by the pulsed Xe lamp's flash profile, a monoexponential fit (R^2 = 0.998) was obtained for the [Eu·L] single crystals. This decay profile (τ = 601 μs) demonstrates that the Eu^{3+} ions occupy a single symmetry site in the DO3A-dppz complex, which corroborates the single, very sharp $^5D_0 \rightarrow {}^7F_0$ peak observed in its emission spectrum (Fig. 6). To expand the Eu[DO3A-dppz] excited-state characterization, photoluminescence decay curves were also recorded for the complex dissolved in water (1 mg ml^{-1}). Biexponential behavior was observed in this case. A first explanation for this phenomenon would be the higher mobility of the complex, showing higher degrees of freedom in solution compared to the single-crystal form. However, such an effect would be identical for all [Eu·L] molecules, and thus the luminescence decay curve would still be monoexponential. A second hypothesis would be the presence of two species of [Eu·L] in solution, *i.e.*, the pristine nonadentate form and one with a higher coordinating number around the Eu^{3+} ions, to which H_2O molecules would be bound. The extra H_2O molecules in the inner coordination sphere could account for the extra vibronic quenching of the excited states, as observed from the curves in Fig. S9. The same behavior could be expected for the NIR-emitting complexes in solution since the coordination chemistry among Ln^{3+} ions is very similar, but it is worth considering that the nonadentate form is still dominant over the higher-coordinated one, as no changes in the $^5D_0 \rightarrow {}^7F_0$ transition of Eu^{3+} were observed when moving from the [Eu·L] single crystal to its dissolved counterpart.

To better illustrate the energy transfer processes happening in the [Eu(DO3A-dppz)] complex, the construction of a Jablonski diagram is necessary. For that, the energies of the singlet (S_1) and triplet (T_1) excited states of the DO3A-dppz ligand had to be measured. Following a previously reported procedure from some of us,[46] the photoluminescence of the analogous [Gd(DO3A-dppz)] complex, dissolved in an ethanol/methanol mixture (4 : 1), was measured at room temperature and at 77 K (Fig. S10). The rise of the emission band centered at ~550 nm at low temperature is assigned to the triplet excited state, while the broad emission band at 448–530 nm is attributed to the singlet excited state. The lowest wavelengths, *i.e.*, the highest energy values from these transitions, were then selected to construct the Jablonski diagram for the [Eu·L] system (Fig. 7). The diagram illustrates that luminescence from both the ligand and the Eu^{3+} ion is possible; however, efficient ligand-to-metal energy transfer ensures high-intensity $^5D_0 \rightarrow {}^7F_{0-4}$ emissions.

According to the relative positions of the energy levels, two different energy transfer pathways can be expected in this system. The first and more prominent is the $T_1 \rightarrow S_0$ [DO3A-

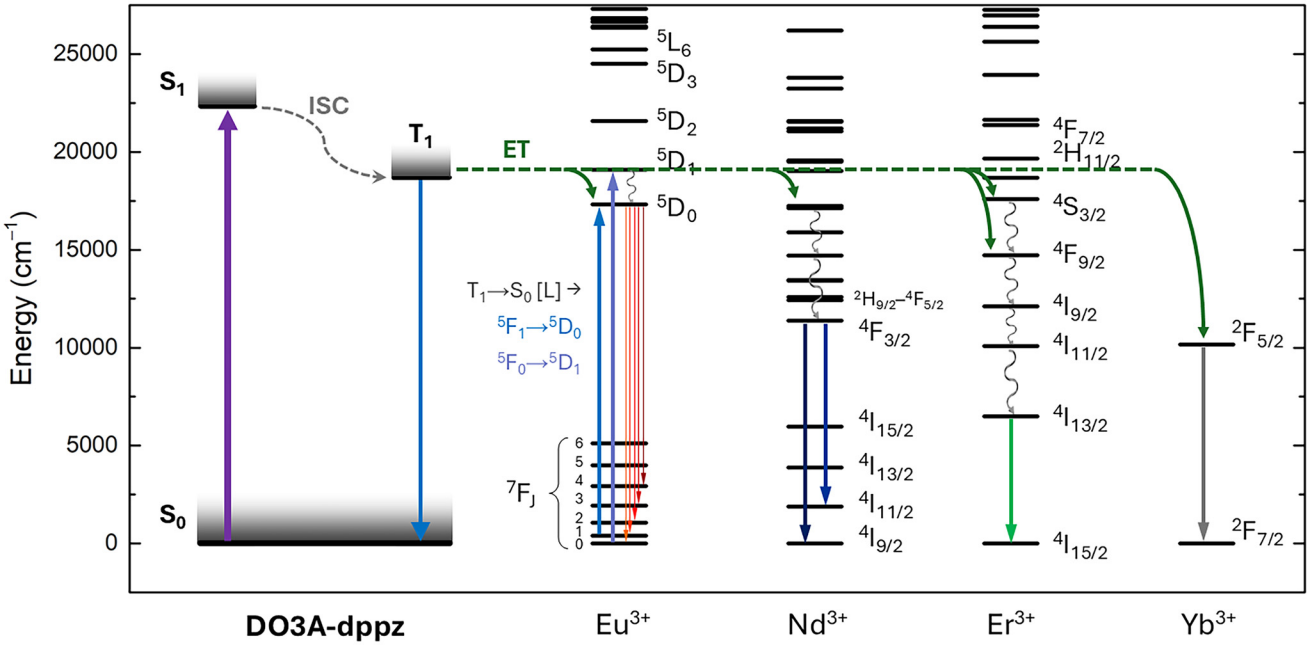

Fig. 7 Jablonski diagram illustrating the energy absorption by the DO3A-dppz ligand ($S_0 \rightarrow S_1$, upward purple arrow), the subsequent $S_1 \rightarrow T_1$ inter-system crossing (ISC, dashed curved arrow), followed by energy transfer (ET, dashed green arrow) to the Eu^{3+} ion, finally leading to the $^5D_0 \rightarrow {}^7F_{0-4}$ emissions (downward red arrows). The downward blue arrow represents the emission from the DO3A-dppz ligand, and the different ligand-to-Eu^{3+} ET pathways are highlighted. The energies of the S_1 and T_1 levels were extracted from Fig. S10.

dppz] → $^5F_0$ → $^5D_1$ [Eu^{3+}] pathway, *i.e.*, exciting the $^5D_1$ level of the Eu^{3+} ions.[47] The second would be the $T_1 \rightarrow S_0$ [DO3A-dppz] → $^5F_1$ → $^5D_0$ [Eu^{3+}] pathway. Direct $^5F_0 \rightarrow {}^5D_0$ sensitization is forbidden by selection rules, but at room temperature, there is a non-negligible electron population on the $^7F_1$ level, which allows a $^5F_1 \rightarrow {}^5D_0$ sensitization.[48] Moreover, a direct transition from the S_1 state cannot be ruled out, as the energy transfer rates for the $S_1 \rightarrow S_0$ [DO3A-dppz] → $^5F_1 \rightarrow {}^5G_2$ [Eu^{3+}] pathway have been reported to be just one order of magnitude lower (~10^7 s^{-1}) compared to those for T_1-based pathways (~10^8 s^{-1}).[48] These results are corroborated by the absence of Tb^{3+} emission in the [Tb(DO3A-dppz)] complex (not shown), since the Tb^{3+} $^5D_4$ state lies at a much higher energy level compared to the Eu^{3+} $^5D_0$ state.[49]

All complexes are moderately soluble in water, with a maximal solubility of 4 mg ml^{-1}. To assess their potential for biomedical applications, the stability of the complexes was tested using UV-Vis spectroscopy by incubating [Eu·L], as an example, in Tris-HCl buffer at 37 °C. The obtained results show sufficient stability of the complex in Tris-HCl buffer (Fig. 8), as no significant spectral changes are observed over a period of 24 h. The major peak at 277 nm can be assigned to a ligand-centered $\pi \rightarrow \pi^*$ transition, while additional peaks at 363 nm and 381 nm are related to $n \rightarrow \pi^*$ transitions.[21,25]

The NIR-emitting [Nd·L] complex was selected as a representative of the series to investigate its interaction with DNA using a SYBR Green I displacement assay in the presence of CT-DNA in Tris-HCl buffer. SYBR Green dyes are widely used in biological experiments, posing significantly decreased potential health

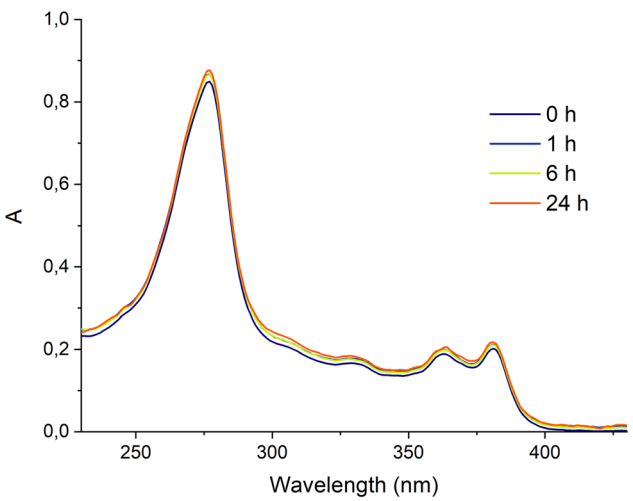

Fig. 8 UV-Vis absorption spectra of the [Eu·L] complex in 1 M Tris-HCl buffer, pH 7.4, measured at 0, 1, 6 and 24 h of incubation at 37 °C.

risks in comparison with the formerly used ethidium bromide. These dyes show enhanced emissions when intercalated into DNA sequences, in contrast to their non-interactive free state. Competition between the presented complexes and SYBR Green I was followed by fluorescence spectroscopy. Unfortunately, the concentration of SYBR Green I is proprietary information, precluding detailed calculations of binding constants.

Our results demonstrate significant interaction of the complex with the model CT-DNA (Fig. 9). A final dilution of

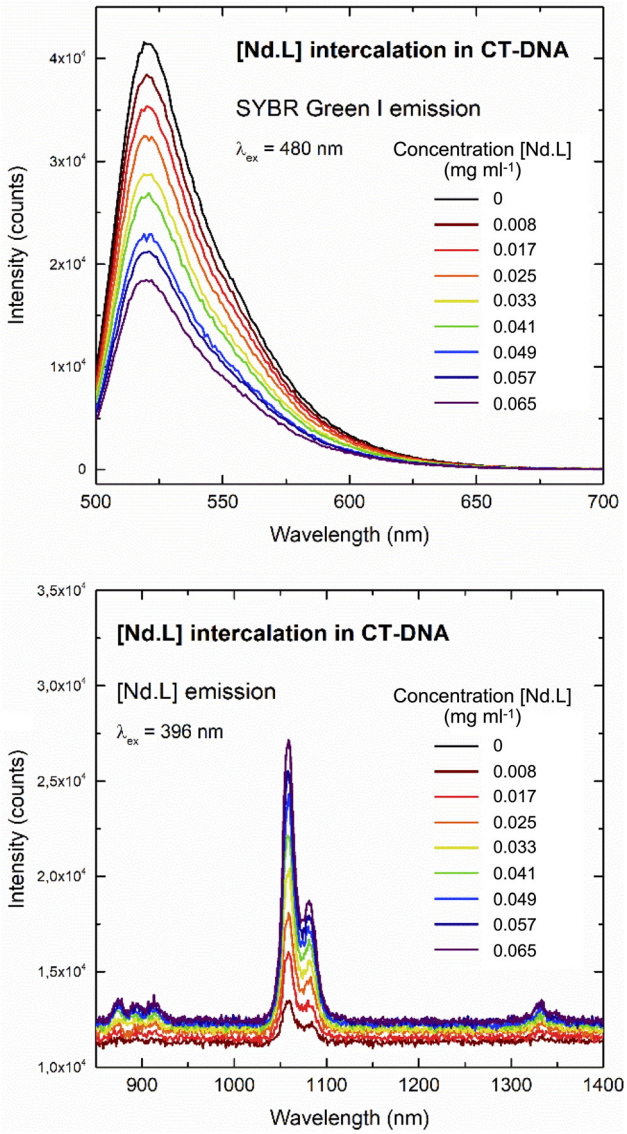

Fig. 9 (Top) Decrease in the emission of SYBR Green I with the addition of the [Nd·L] complex, demonstrating the competition between the SYBR Green I dye and the [Nd·L] complex. (Bottom) Increase in the [Nd·L] emission intensity as a function of its concentration.

the SYBR Green I to a 2× concentrate (see Experimental) was identified as optimum for effective interaction of the dye with the available amount of CT-DNA, while maintaining sufficient fluorescence response and effective competition with the complex. Even though the precise affinity is affected by the concentration, a considerable decrease in the emission of SYBR Green I is already observed with initial increments of the complex. Upon addition of 5 μl of the 2.5 mg ml^{-1} [Nd·L] solution, the integrated SYBR Green I emission decreased by 7.5%. After adding the entire 40 μl of [Nd·L], the emission dropped to merely 55% of its initial value. Similar results were found when conducting an analogous experiment with the visible-light-emitting Eu^{3+} complex (Fig. S11), *i.e.*, 8.9% and 47% decreases in the SYBR Green I emission intensity after addition of 5 and 40 μl of the 2.5 mg ml^{-1} [Eu·L] solution, respectively. While such a decrease in emission cannot be explained only by the dilution factor of the CT-DNA with the incorporated dye, smaller steps in the emission decrease can be explained by competition between the progressively released dye and the complex. To verify whether the [Nd·L] can potentially be used as an NIR DNA probe in solution, simultaneously, the Nd^{3+} complex emission was recorded during the experiments. While the SYBR Green I emission decreases in intensity with subsequent additions of [Nd·L], the emission intensity of the Nd^{3+} complex increases in a linear trend as a function of its concentration in the environment. These results further validate the CT-DNA–SYBR Green I intercalation mechanism and the replacement of SYBR Green I molecules by [Nd·L], confirming the potential use of [Nd·L] as a NIR probe.

3 Experimental

3.1 Ligand and complex synthesis

A modified approach to the reported procedures was performed in synthesis steps, leading to the obtained complexes,[21,22,41] *t*Bu-DO3A·HBr was synthesized according to a previously reported procedure.[50] Details of the synthesis of the reported molecules 2-methyl-1,10-phenanthroline and 2-methyl-1,10-phenanthroline-5,6-dione are provided in the SI. ^{1}H and ^{13}C NMR spectra were recorded at room temperature using Bruker Avance I 300 MHz and Bruker Avance II 400 MHz spectrometers. Chemical shifts are reported in ppm and are referenced to the internal standard TMS ($\delta_H = \delta_C = 0.00$ ppm) or the residual solvent peaks of $CDCl_3$ ($\delta_H = 7.26$ ppm and $\delta_C = 77.16$ ppm) and D_2O ($\delta_H = 4.79$ ppm). The unit for coupling constants J is Hz with 1 decimal point accuracy for ^{1}H spectra. Mass spectra were obtained by direct injection on an Agilent 1100 Series HPLC and on an Agilent 6220A time-of-flight HRMS using an ESI/APCI-multimode ionization source. All ^{1}H, ^{13}C NMR and (HR)MS spectra can be found in the SI.

3-Methyl-dipyrido[3,2-*a*:2′,3′-*c*]phenazine (Me-dppz). *o*-Phenylenediamine (670 mg, 6.20 mmol) was dissolved in 20 ml of absolute EtOH and added to a stirred solution of Me-phendione (1.40 g, 6.20 mmol) in 80 ml of absolute EtOH at reflux. The reaction mixture was refluxed for 4 h. After cooling down, the solution was concentrated by evaporation and the product was recrystallized from absolute EtOH. An off-white powder was collected, washed with diethyl ether and dried in a vacuum oven (1.40 g, 76%). **^{1}H NMR (400 MHz, $CDCl_3$):** δ = 2.98 (s, 3H, CH_3), 7.62 (d, 1H, J = 8.2 Hz, H2), 7.74 (dd, 1H, J = 8.1, 4.5 Hz, H7), 7.87 (m, 2H, H10 and H13), 8.27 (m, 2H, H11 and H12), 9.27 (dd, 1H, J = 4.5, 1.8 Hz, H6), 9.43 (d, 1H, J = 8.2 Hz, H1), 9.57 (dd, 1H, J = 8.1, 1.8 Hz, H8). **^{13}C{^{1}H} NMR (100 MHz, $CDCl_3$):** δ = 25.9 (CH_3), 123.9 (C7), 124.6 (C2), 125.3 (Cq2), 127.6 (Cq5), 129.5 (C12), 129.6 (C11), 130.4 (C10), 130.6 (C13), 133.9 (C1), 134.0 (C8), 140.9 (Cq4), 141.3 (Cq3), 142.3 (Cq7), 142.5 (Cq8), 147.9 (Cq1), 148.4 (Cq6), 152.7 (C6), 162.3 (C3). **HRMS(+):** 297.1142 ([M + H]$^+$ calc. 297.1135).

3-Carboxyaldehyde-dipyrido[3,2-*a*:2′,3′-*c*]phenazine (O=Me-dppz). Me-dppz (900 mg, 3.04 mmol) was dissolved in 250 ml of 1,4-dioxane. Selenium(IV) dioxide (337 mg, 3.04 mmol, 1 eq.) was added and the reaction mixture was stirred for 4 h at reflux. After cooling down to RT, the mixture was filtered over Celite, solvents were evaporated and the obtained crude solid was used for the next step without extra purification (890 mg, 94%). **^{1}H NMR (400 MHz, $CDCl_3$):** δ = 7.84 (dd, 1H, J = 8.1, 4.4 Hz, H7), 7.96 (m, 2H, H11 and H12), 8.35 (m, 2H, H10 and H13), 8.40 (d, 1H, J = 8.2 Hz, H1), 9.33 (dd, 1H, J = 4.4, 1.8 Hz, H6), 9.64 (dd, 1H, J = 8.1, 1.8 Hz, H8), 9.79 (dd, 1H, J = 8.2, 0.9 Hz, H2), 10.61 (d, 1H, J = 0.9 Hz, CHO). **^{13}C{^{1}H} NMR (100 MHz, $CDCl_3$):** δ = 121.1 (C1), 124.8 (C7), 128.2 (Cq5), 129.7 (C13), 129.9 (C10), 130.8 (Cq2), 131.2 (C12), 131.6 (C11), 134.1 (C8), 135.4 (C2), 140.2 (Cq3), 141.5 (Cq4), 142.7 (Cq8), 143.0 (Cq7), 147.7 (Cq6), 148.5 (Cq1), 153.0 (C6), 154.1 (C3), 193.9 (CHO). **HRMS(+):** 311.0931 ([M + H]$^+$ calc. 311.0927).

3-Hydroxymethyl-dipyrido[3,2-*a*:2′,3′-*c*]phenazine (OH-Me-dppz). The crude material from the previous step (880 mg, 2.84 mmol) was dissolved in a 240 ml mixture of $CHCl_3$ and absolute EtOH (2 : 1, v/v). Sodium borohydride (215 mg, 5.68 mmol, 2 eq.) was added and the reaction mixture was stirred for 3 h at reflux. After cooling down, the solvents were evaporated, and the residue was dissolved in 200 ml of $CHCl_3$ and washed twice with 100 ml of 10% Na_2CO_3. The organic part was dried using anhydrous sodium sulfate, solids were separated, and the filtrate was evaporated to give a pale pink solid (816 mg, 92%), which was used in the next step without further purification. **^{1}H NMR (400 MHz, $CDCl_3$):** δ = 5.22 (s, 1H, CH_2), 7.75 (dd, 1H, J = 8.1, 4.5 Hz, H7), 7.85 (d, 1H, J = 8.3 Hz, H2), 7.90 (m, 2H, H10 and H13), 8.28 (m, 2H, H11 and H12), 9.20 (dd, 1H, J = 4.5, 1.8 Hz, H6), 9.51 (d, 1H, J = 8.3 Hz, H1), 9.56 (dd, 1H, J = 8.1, 1.8 Hz, H8). **^{13}C{^{1}H} NMR (100 MHz, $CDCl_3$):** δ = 65.9 (CH_2), 121.6 (C2), 124.2 (C7), 126.5 (Cq2), 127.8 (Cq5), 129.6 (C12), 129.6 (C11), 130.7 (C13), 130.8 (C10), 134.1 (C8), 134.5 (C1), 140.8 (Cq6), 141.0 (Cq1), 142.4 (Cq7), 142.6 (Cq8), 147.3 (Cq4), 148.0 (Cq3), 152.4 (C6), 163.6 (C3). **HRMS(+):** 313.1081 ([M + H]$^+$ calc. 313.1084).

3-Bromomethyl-dipyrido[3,2-*a*:2′,3′-*c*]phenazine (Br-Me-dppz). The material from the previous step (800 mg, 2.56 mmol) was dissolved in 240 ml of $CHCl_3$. Phosphorus tribromide (0.73 ml, 7.68 mmol, 3 eq.) was diluted in 5 ml of $CHCl_3$ and dropwise added to the reaction mixture at reflux, forming a precipitate and turning the reaction mixture violet. The reaction was left to stir for 4 h at reflux temperature, resulting in a dark yellow solution without any visible precipitate. After cooling down, 150 ml of 10% Na_2CO_3 was added, the organic phase was separated, and the water phase was extracted with 2 × 100 ml of $CHCl_3$. The organic phases were combined and dried with anhydrous sodium sulfate, the solids were separated and the filtrate was evaporated. The crude residue was purified by column chromatography on silica gel (1% MeOH : DCM isocratic solution; R_f = 0.3, 5% MeOH : DCM), yielding a colorless solid of Br-Me-dppz (355 mg, 37%). **^{1}H NMR (400 MHz, $CDCl_3$):** δ = 5.01 (s, 1H, CH_2), 7.81 (dd, 1H, J = 8.1, 4.5 Hz, H7), 7.94 (m, 2H, H10 and H13), 8.04 (d, 1H, J = 8.3 Hz, H2), 8.37 (m, 2H, H11 and H12), 9.33 (dd, 1H, J = 4.5, 1.8 Hz, H6), 9.68 (dd, 1H, J = 8.1, 1.8 Hz, H8), 9.69 (d, 1H, J = 8.3 Hz, H1). **^{13}C{^{1}H} NMR (100 MHz, $CDCl_3$):** δ = 34.3 (CH_2), 124.4 (C7), 124.8 (C2), 127.0 (Cq2), 128.0 (Cq5), 129.7 (C12), 129.7 (C13), 131.0 (2C, C10 and C13), 134.4 (C8), 135.2 (C1), 140.7 (Cq4), 140.9 (Cq3), 142.6 (Cq8), 142.7 (Cq7), 147.7 (Cq1), 147.7 (Cq6), 152.5 (C6), 160.1 (C3). **HRMS(+):** 375.0227 ([M + H]$^+$ calc. 375.0240).

1-(3-Methyl-dipyrido[3,2-*a*:2′,3′-*c*]phenazine)-4,7,10-tris(*tert*-butoxycarbonyl)-1,4,7,10-tetraazacyclododecane (*t*Bu-DO3A-dppz). *t*Bu-DO3A·HBr (476 mg, 0.80 mmol) was dissolved in 60 ml of MeCN, followed by the addition of potassium carbonate (663 mg, 4.80 mmol, 6 eq.) and a catalytic amount of KI (0.5 mg). Br-Me-dppz (300 mg, 0.80 mmol, 1 eq.) was dissolved in 60 ml of DCM and added to the reaction mixture, which was stirred at 60 °C overnight. The next day, after cooling to RT, the mixture was filtered over Celite, the solids were washed with DCM and the solvents from the filtrate were evaporated. The crude product was purified by reverse-phase flash column chromatography (C18 column, A: H_2O with 0.1% TFA and B: MeCN with 0.1% TFA, gradient elution of A : B 100 : 0 to 0 : 100 over 25 min at 50 ml min^{-1}, PDA detection), giving an off-white solidifying oil (705 mg, 85%, calc. with *t*Bu-DO3A-dppz·2TFA). **^{1}H NMR (400 MHz, $CDCl_3$):** δ = 1.11 (s, 18H, CH_3), 1.48 (s, 9H, CH_3), 2.48 (br m, 4H, CH_2 ring), 2.70 (br m, 6H, CH_2 ring), 2.86 and 2.90 (s & s, 4H, CH_2), 3.11 (br m, 6H, CH_2 ring), 3.49 and 3.53 (s & s, 2H, CH_2), 4.12 (br s, 2H, dppz-CH_2), 7.81 (d, 1H, J = 8.3 Hz, H2), 7.83 (dd, 1H, J = 8.1, 4.5 Hz, H7), 7.96 (m, 2H, H10 and H13), 8.36 (m, 2H, H11 and H12), 8.89 (dd, 1H, J = 4.5, 1.8 Hz, H6), 9.64 (d, 1H, J = 8.3 Hz, H1), 9.64 (dd, 1H, J = 8.1, 1.8 Hz, H8). **^{13}C{^{1}H} NMR (100 MHz, $CDCl_3$):** δ = 27.9 (CH_3), 28.2 (CH_3), 29.8 (C *t*Bu), 29.8 (C *t*Bu), 56.2 (CH_2 ring), 57.4 (CH_2 ring), 60.4 (CH_2 ring), 81.8 (CH_2 ac), 82.8 (CH_2 ac), 124.2 (C7), 124.4 (C2), 126.7 (Cq), 128.3 (Cq), 129.7 (C12), 129.7 (C13), 131.1 (C10), 131.2 (C13), 134.6 (C8), 134.9 (C1), 140.7 (Cq), 140.9 (Cq), 142.7 (Cq), 142.8 (Cq), 147.3 (Cq), 147.8 (Cq), 152.1 (C6), 161.8 (C3), 172.8 (CH_2 dppz). **HRMS(+):** 809.4699 ([M + H]$^+$ calc. 809.4709).

1-(3-Methyl-dipyrido[3,2-*a*:2′,3′-*c*]phenazine)-4,7,10-tris(carboxymethyl)-1,4,7,10-tetraazacyclododecane (DO3A-dppz, L). The *t*Bu-DO3A-dppz material from the previous step (141 mg, 0.136 mmol) was dissolved in 40 ml of DCM, followed by addition of 20 ml of trifluoroacetic acid. The mixture was stirred overnight at RT. The next day, the solvents were evaporated and the residue was redissolved and evaporated in 3 × 20 ml of DCM to remove the excess solvents and byproducts. The crude residue was used without further purification in the next step (137 mg, DO3A-dppz·*x*TFA). **^{1}H NMR (400 MHz, D_2O):** δ = 2.74–3.90 (br m, 24H, CH_2 alkyl), 7.81 (br s, 4H, ar), 8.06 (br s, 1H, ar), 8.28 (br s, 1H, ar), 8.86 (br s, 1H, ar), 9.15 (br s, 1H, ar), 9.51 (br s, 1H, ar). **MS(+):** 641.2 ([M + H]$^+$ calc. 641.3).

General procedure of the synthesis of 1-(3-methyldipyrido[3,2-*a*:2′,3′-*c*]phenazine)-4,7,10-tris(carboxymethyl)1,4,7,10-tetraazacyclododecane lanthanide complex ([Ln(DO3A-dppz)], Ln·L). The material from the previous step was dissolved in 80 ml of an H_2O : MeOH (1 : 1, v/v) mixture, and 20 ml of the

mixture with the DO3A-dppz ligand (0.034 mmol) was transferred to a flask with 1.5 eq. of the corresponding $LnCl_3{\cdot}6H_2O$ (approx. 20 mg). The pH of the solution was adjusted to 5.5 using 1 M KOH and the reaction mixture was stirred overnight at 80 °C, with readjustment of the pH to 5.5, if necessary. The next day, the pH was increased to 10 and the reaction was left to stir for 1 h. After cooling down, solids were filtered off using a syringe filter, the volatiles from the filtrate were evaporated, and the residue was purified by reverse-flash column chromatography (C18 column, A: H_2O and B: MeOH, gradient change of A to B over 5 min, at 50 ml min^{-1}, PDA detection). The fractions containing the final complex were combined, organic solvents were removed and the residue was freeze-dried to obtain a powder of the respective [Ln(DO3A-dppz)] complex.

[La(DO3A-dppz)]: yellow powder (17.4 mg, 66%). **HRMS(+):** 777.1695 ($[M + H]^+$ calc. 777.1659).

[Ce(DO3A-dppz)]: yellow powder (19.1 mg, 72%). **HRMS(+):** 778.1646 ($[M + H]^+$ calc. 778.1650).

[Pr(DO3A-dppz)]: off-white powder (16.9 mg, 68%). **HRMS (+):** 779.1676 ($[M + H]^+$ calc. 779.1672).

[Nd(DO3A-dppz)]: off-white powder (16.3 mg, 61%). **HRMS (+):** 780.1654 ($[M + H]^+$ calc. 780.1673).

[Sm(DO3A-dppz)]: off-white powder (20.6 mg, 77%). **HRMS (+):** 790.1776 ($[M + H]^+$ calc. 790.1793).

[Eu(DO3A-dppz)]: yellow powder (18.8 mg, 71%). **HRMS(+):** 791.1786 ($[M + H]^+$ calc. 791.1808).

[Gd(DO3A-dppz)]: off-white powder (21.4 mg, 79%). **HRMS (+):** 796.1799 ($[M + H]^+$ calc. 796.1837).

[Tb(DO3A-dppz)]: off-white powder (18.7 mg, 69%). **HRMS (+):** 797.1823 ($[M + H]^+$ calc. 797.1849).

[Dy(DO3A-dppz)]: off-white powder (16.9 mg, 62%). **HRMS (+):** 802.1883 ($[M + H]^+$ calc. 802.1888).

[Ho(DO3A-dppz)]: off-white powder (15.5 mg, 57%). **HRMS (+):** 803.1894 ($[M + H]^+$ calc. 803.1899).

[Er(DO3A-dppz)]: off-white powder (20.8 mg, 76%). **HRMS (+):** 804.1883 ($[M + H]^+$ calc. 804.1899).

[Tm(DO3A-dppz)]: off-white powder (19.2 mg, 70%). **HRMS (+):** 807.1917 ($[M + H]^+$ calc. 807.1938).

[Yb(DO3A-dppz)]: off-white powder (18.9 mg, 69%). **HRMS (+):** 812.1972 ($[M + H]^+$ calc. 812.1984).

[Lu(DO3A-dppz)]: off-white powder (21.1 mg, 76%). **HRMS (+):** 813.1996 ($[M + H]^+$ calc. 813.2004).

3.2 Single-crystal X-ray diffraction

Single crystals of Me-phen were obtained directly from the filtrate and single crystals of organic intermediates Br-Me-dppz and *t*Bu-DO3A-dppz were obtained using a vapor diffusion technique with a combination of $CHCl_3$/hexane or DCM/pentane. Single crystals of the [Ln(DO3A-dppz)] complexes were grown by dissolving the material at reflux in MeOH and subsequent slow crystallization over the next 1–3 days. Single-crystal X-ray diffraction data were collected using a Rigaku Oxford Diffraction SuperNova Dual Source (Cu and Mo) diffractometer equipped with an Atlas CCD detector using ω scans and Cu K_α or Mo K_α radiation. Data reductions were achieved with Rigaku CrysAlisPro software (Rigaku Oxford Diffraction).[51] The crystal structures were solved by intrinsic phasing using the ShelXT program[52] and the structures were refined by the full-matrix least-squares method using the ShelXL program.[53] Both ShelXT and ShelXL are implemented within the Olex2 interface.[54] All non-hydrogen atoms were refined anisotropically and hydrogen atoms were fixed geometrically and refined using a riding model. In the case of *t*Bu-DO3A-dppz, one highly disordered trifluoroacetate counterion and 4 DCM solvate molecules were masked and in the case of the final complexes, 4–5 highly disordered MeOH molecules were masked using a solvent mask in the Olex2 interface.[54] All crystallographic data can be found in the SI (Table S1).

3.3 Photoluminescence experiments

Photoluminescence excitation and emission spectra were recorded with an Edinburgh Instruments FLSP1000 UV/Vis-NIR spectrofluorometer using a 450 W xenon lamp as the steady state excitation source, a Hamamatsu R928P (200–900 nm) detector, and a Hamamatsu R5509-72 (850–1700 nm) photomultiplier operating at −80 °C. Photoluminescence decay curves of the NIR emitting samples in the microsecond domain were obtained by excitation with a pulsed wavelength-tunable (Carlsbad, CA, USA) Opotek Opolette 355 LD optical parametric oscillator (OPO) with a repetition rate of 20 Hz and a temporal pulse width of around 6 ns. The time-dependent signal was processed in a multichannel scaler (MCS). Decay curves of the Eu^{3+} samples were measured using an FLSP920 system equipped with a 150 W pulsed xenon lamp as the excitation source and a Hamamatsu R928P detector. The data for the Nd^{3+} and Er^{3+} samples were too short to detect using this system. Photoluminescence excitation and emission spectra of the Nd^{3+}, Er^{3+}, Yb^{3+} and Eu^{3+} complexes were obtained in both the solid state (powder) and an aqueous solution.

3.4 Stability study

UV-Vis spectra were recorded using an Implen™ NanoPhotometer™ NP80 Nano-Volume and Cuvette UV-Vis spectrophotometer. 0.5 mg of [Eu·L] was dissolved in 5 ml of 1 M Tris-HCl buffer at pH 7.4 and incubated at 37 °C. An aliquot of 300 µl was taken from the stock solution at 0, 1, 6 and 24 h after the start of incubation, diluted to 3 ml using the buffer solution in a quartz cuvette with a path length of 10 mm, and the UV-Vis spectra were recorded in the range of 200–900 nm.

3.5 Calf-thymus DNA interaction tests

Commercially available SYBR™ Green I solution in DMSO (10 000× concentrate) was diluted to 100× concentrate using DMSO, with further dilution to a final 2× concentrate using Tris-HCl buffer (pH 7.4). The stock solution of calf-thymus DNA (Merck, fibers) was prepared by slowly dissolving 1.33 mg of CT-DNA in 1 ml of Tris-HCl buffer, with further dilution using Tris-HCl buffer to a final concentration of 1.33 µg ml^{-1}. The [Nd·L] and [Eu·L] solutions were prepared by dissolving 1.25 mg of the compound in 0.5 ml of Tris-HCl buffer to a final concentration of 2.50 mg ml^{-1}. A HELLMA quartz cuvette with a path

length of 10 mm was filled with 1.25 ml of CT-DNA solution, 0.25 ml of the SYBR Green I solution, and the corresponding amount of the complex solution in 5 μl increments. The SYBR Green was excited at 480 nm and the emission profile was recorded in the range of 500–700 nm with an observed maximum at 520 nm. Simultaneously, the [Nd·L] (λ_{ex} = 396 nm) and [Eu·L] (λ_{ex} = 398 nm) emissions were recorded in the ranges of 850–1400 nm and 500–750 nm, respectively.

4 Conclusions

We have obtained the new ligand DO3A-dppz and synthesized all feasible lanthanide complexes [Ln(DO3A-dppz)]. All complexes were successfully characterized by SCXRD, showing the development of isomers from [Ho·L] onward. Photoluminescence studies correlate with the expected results in terms of excitation and emission for [Nd·L], [Er·L], [Yb·L] and [Eu·L], achieving a decay time of 5.0 μs with [Yb·L]. All complexes are weakly soluble in water, with good stability investigated by incubation in Tris-HCl buffer. In the end, interaction with the model CT-DNA was proved by a SYBR™ Green I displacement assay using [Nd·L] as a representative of the series. In the future, we plan to co-crystallize selected complexes with DNA oligonucleotides to prove the potential of intercalation or other interactions with the DNA fragments. Other opportunities include modifications of the ligand to further increase solubility; however, these modifications might bring a downside of decreased capability of interaction with DNA. Altogether, these complexes provide opportunities for further study and development towards utilization in biomedical applications.

Author contributions

M. B.: conceptualization, formal analysis, lead investigation, project administration, validation, visualization, and writing – original draft; J. Š.: investigation and validation; S. B.: formal analysis and writing – review & editing; S. P.: investigation; M. L.: investigation and formal analysis; I. P. M.: investigation, formal analysis and writing – review & editing; A. M. K.: funding acquisition and resources; K. V. H.: conceptualization, funding acquisition, resources, supervision, and writing – review & editing.

Conflicts of interest

There are no conflicts to declare.

Data availability

Supplementary information (SI): NMR, MS and HRMS spectra, experimental details for the synthesis of Me-phen and Me-phendione, crystallographic data, photoluminescence spectra and decay profiles. See DOI: https://doi.org/10.1039/d6dt00235h.

CCDC 2515749–2515765 contain the supplementary crystallographic data for this paper.[55a–q]

Acknowledgements

M. B. and K. V. H. acknowledge the Research Foundation – Flanders (FWO) (project no. G099319N) and the Special Research Fund (BOF) – UGent (project no. BOF23/CDV/018) for funding. We thank the NMR Expertise Centre, Ghent University for providing access to its 300 MHz and 400 MHz spectrometers (project no. FWO I006920N and BOF. BAS.2022.0023.01). This work is part of a project that has received funding from the European Research Council (ERC) under the European Union's Horizon 2020 Research and Innovation Programme (grant agreement no. 945945). We are thankful to Prof. A. Meijerink (Utrecht University) for access to the PL setup and Prof. J. Kotek (Charles University) for access to the laboratory.

References

1 R. D. Teo, J. Termini and H. B. Gray, *J. Med. Chem.*, 2016, **59**, 6012–6024.
2 Q. Zhang, S. O'Brien and J. Grimm, *Nanotheranostics*, 2022, **6**, 184–194.
3 S. Lacerda and E. Tóth, *ChemMedChem*, 2017, **12**, 883–894.
4 H. U. Rashid, K. Yu and J. Zhou, *J. Struct. Chem.*, 2013, **54**, 223–249.
5 X. Wang, H. Chang, J. Xie, B. Zhao, B. Liu, S. Xu, W. Pei, N. Ren, L. Huang and W. Huang, *Coord. Chem. Rev.*, 2014, **273–274**, 201–212.
6 U. Cho and J. K. Chen, *Cell Chem. Biol.*, 2020, **27**, 921–936.
7 E. J. New, D. Parker, D. G. Smith and J. W. Walton, *Curr. Opin. Chem. Biol.*, 2010, **14**, 238–246.
8 J. R. Morrow, L. A. Buttrey, V. M. Shelton and K. A. Berback, *J. Am. Chem. Soc.*, 1992, **114**, 1903–1905.
9 C. Xu and X. Qu, *NPG Asia Mater.*, 2014, **6**, e90.
10 R. A. Jones, A. J. Gnanam, J. F. Arambula, J. N. Jones, J. Swaminathan, X. Yang, D. Schipper, J. W. Hall, L. J. DePue, Y. Dieye, J. Vadivelu, D. J. Chandler, E. M. Marcotte, J. L. Sessler, L. I. R. Ehrlich and K. A. Brown, *Faraday Discuss.*, 2014, **175**, 241–255.
11 K. Mishiro, H. Hanaoka, A. Yamaguchi and K. Ogawa, *Coord. Chem. Rev.*, 2019, **383**, 104–131.
12 M. Hasegawa, H. Ohmagari, H. Tanaka and K. Machida, *J. Photochem. Photobiol., C*, 2022, **50**, 100484.
13 J.-C. G. Bünzli, *Coord. Chem. Rev.*, 2015, **293–294**, 19–47.
14 K. Binnemans, *Chem. Rev.*, 2009, **109**, 4283–4374.
15 I. V. Barbosa, L. J. Maia, A. Ibanez and G. Dantelle, *Opt. Mater.: X*, 2023, **18**, 100236.

16 *Transparency in Biology: Making the Invisible Visible*, ed. K. Soga, M. Umezawa and K. Okubo, Springer Singapore, 2021.
17 M. P. Cabral Campello, E. Palma, I. Correia, P. M. R. Paulo, A. Matos, J. Rino, J. Coimbra, J. C. Pessoa, D. Gambino, A. Paulo and F. Marques, *Dalton Trans.*, 2019, **48**, 4611–4624.
18 K. Singh, S. Banerjee and A. K. Patra, *RSC Adv.*, 2015, **5**, 107503–107513.
19 X.-X. Peng, X.-F. Zhu and J.-L. Zhang, *J. Inorg. Biochem.*, 2020, **209**, 111118.
20 J.-C. G. Bünzli, *Chem. Rev.*, 2010, **110**, 2729–2755.
21 A. Savić, A. M. Kaczmarek, R. Van Deun and K. Van Hecke, *Molecules*, 2020, **25**, 5309.
22 R. A. Poole, G. Bobba, M. J. Cann, J.-C. Frias, D. Parker and R. D. Peacock, *Org. Biomol. Chem.*, 2005, **3**, 1013–1024.
23 G. Panigrahi, S. Pradhan, N. Shukla and A. K. Patra, *Chem. – Eur. J.*, 2025, **31**, e02440.
24 Q. Sun, P. Yan, W. Niu, W. Chu, X. Yao, G. An and G. Li, *RSC Adv.*, 2015, **5**, 65856–65861.
25 S. Dasari, Z. Abbas, P. Kumar and A. K. Patra, *CrystEngComm*, 2016, **18**, 4313–4322.
26 Z. Abbas, P. Singh, S. Dasari, S. Sivakumar and A. K. Patra, *New J. Chem.*, 2020, **44**, 15685–15697.
27 S. Dasari and A. K. Patra, *Dalton Trans.*, 2015, **44**, 19844–19855.
28 S. Dasari, S. Singh, S. Sivakumar and A. K. Patra, *Chem. – Eur. J.*, 2016, **22**, 17387–17396.
29 S. Fan, X. Yao, J. Li, W. Li and G. Li, *J. Lumin.*, 2018, **203**, 473–480.
30 S. Dasari, S. Singh, P. Kumar, S. Sivakumar and A. K. Patra, *Eur. J. Med. Chem.*, 2019, **163**, 546–559.
31 R. M. Hartshorn and J. K. Barton, *J. Am. Chem. Soc.*, 1992, **114**, 5919–5925.
32 K. T. McQuaid and C. J. Cardin, in *The eyes have it: Using X-ray crystallography to determine the binding modes of medically relevant ruthenium/DNA complexes*, Elsevier, 2020, pp. 393–424.
33 M. D. Pozza, P. Mesdom, A. Abdullrahman, T. D. Prieto Otoya, P. Arnoux, C. Frochot, G. Niogret, B. Saubaméa, P. Burckel, J. P. Hall, M. Hollenstein, C. J. Cardin and G. Gasser, *Inorg. Chem.*, 2023, **62**, 18510–18523.
34 K. McQuaid, H. Abell, S. P. Gurung, D. R. Allan, G. Winter, T. Sorensen, D. J. Cardin, J. A. Brazier, C. J. Cardin and J. P. Hall, *Angew. Chem., Int. Ed.*, 2019, **58**, 9881–9885.
35 K. McQuaid, J. P. Hall, L. Baumgaertner, D. J. Cardin and C. J. Cardin, *Chem. Commun.*, 2019, **55**, 9116–9119.
36 C. J. Cardin, J. M. Kelly and S. J. Quinn, *Chem. Sci.*, 2017, **8**, 4705–4723.
37 P. M. Keane, F. E. Poynton, J. P. Hall, I. V. Sazanovich, M. Towrie, T. Gunnlaugsson, S. J. Quinn, C. J. Cardin and J. M. Kelly, *Angew. Chem., Int. Ed.*, 2015, **54**, 8364–8368.
38 J. P. Hall, D. Cook, S. R. Morte, P. McIntyre, K. Buchner, H. Beer, D. J. Cardin, J. A. Brazier, G. Winter, J. M. Kelly and C. J. Cardin, *J. Am. Chem. Soc.*, 2013, **135**, 12652–12659.
39 H. Niyazi, J. P. Hall, K. O'Sullivan, G. Winter, T. Sorensen, J. M. Kelly and C. J. Cardin, *Nat. Chem.*, 2012, **4**, 621–628.
40 S. Pradhan, N. Shukla, G. Panigrahi and A. K. Patra, *Chem. Commun.*, 2025, **61**, 1886–1889.
41 M. Wosińska-Hrydczuk and J. Skarżewski, *Heteroat. Chem.*, 2019, 2381208.
42 C. J. Chandler, L. W. Deady and J. A. Reiss, *J. Heterocycl. Chem.*, 1981, **18**, 599–601.
43 J. Kotek, J. Rudovský, P. Hermann and I. Lukeš, *Inorg. Chem.*, 2006, **45**, 3097–3102.
44 W. Thor, A. N. Carneiro Neto, R. T. Moura Jr., K.-L. Wong and P. A. Tanner, *Coord. Chem. Rev.*, 2024, **517**, 215927.
45 K. M. Smith, M. F. Reid, M. J. Sellars and R. L. Ahlefeldt, *Phys. Rev. B*, 2022, **105**, 125141.
46 A. M. Kaczmarek, Y.-Y. Liu, M. K. Kaczmarek, H. Liu, F. Artizzu, L. D. Carlos and P. Van Der Voort, *Angew. Chem., Int. Ed.*, 2020, **59**, 1932–1940.
47 O. L. Malta, *J. Non-Cryst. Solids*, 2008, **354**, 4770–4776.
48 L. Blois, A. N. C. Neto, O. L. Malta and H. F. Brito, *J. Lumin.*, 2022, **247**, 118862.
49 W. T. Carnall, H. Crosswhite and H. M. Crosswhite, U.S. Department of Energy Office of Scientific and Technical Information, 1978, pp. 1–38.
50 B. Jagadish, G. L. Brickert-Albrecht, G. S. Nichol, E. A. Mash and N. Raghunand, *Tetrahedron Lett.*, 2011, **52**, 2058–2061.
51 *CrysAlisPro Software System*, Rigaku Corporation, Oxford, UK, 2023.
52 G. M. Sheldrick, *Acta Crystallogr., Sect. A: Found. Adv.*, 2015, **71**, 3–8.
53 G. M. Sheldrick, *Acta Crystallogr., Sect. C: Struct. Chem.*, 2015, **71**, 3–8.
54 O. V. Dolomanov, L. J. Bourhis, R. J. Gildea, J. A. K. Howard and H. Puschmann, *J. Appl. Crystallogr.*, 2009, **42**, 339–341.
55 (*a*) CCDC 2515749: Experimental Crystal Structure Determination, 2026, DOI: 10.5517/ccdc.csd.cc2qfv67; (*b*) CCDC 2515750: Experimental Crystal Structure Determination, 2026, DOI: 10.5517/ccdc.csd.cc2qfv78; (*c*) CCDC 2515751: Experimental Crystal Structure Determination, 2026, DOI: 10.5517/ccdc.csd.cc2qfv89; (*d*) CCDC 2515752: Experimental Crystal Structure Determination, 2026, DOI: 10.5517/ccdc.csd.cc2qfv9b; (*e*) CCDC 2515753: Experimental Crystal Structure Determination, 2026, DOI: 10.5517/ccdc.csd.cc2qfvbc; (*f*) CCDC 2515754: Experimental Crystal Structure Determination, 2026, DOI: 10.5517/ccdc.csd.cc2qfvcd; (*g*) CCDC 2515755: Experimental Crystal Structure Determination, 2026, DOI: 10.5517/ccdc.csd.cc2qfvdf; (*h*) CCDC 2515756: Experimental Crystal Structure Determination, 2026, DOI: 10.5517/ccdc.csd.cc2qfvfg; (*i*) CCDC 2515757: Experimental Crystal Structure Determination, 2026, DOI: 10.5517/ccdc.csd.cc2qfvgh; (*j*) CCDC 2515758: Experimental Crystal Structure Determination, 2026, DOI: 10.5517/ccdc.csd.cc2qfvhj; (*k*) CCDC 2515759: Experimental Crystal Structure Determination, 2026, DOI: 10.5517/ccdc.csd.cc2qfvjk;

(*l*) CCDC 2515760: Experimental Crystal Structure Determination, 2026, DOI: 10.5517/ccdc.csd.cc2qfvkl; (*m*) CCDC 2515761: Experimental Crystal Structure Determination, 2026, DOI: 10.5517/ccdc.csd.cc2qfvlm; (*n*) CCDC 2515762: Experimental Crystal Structure Determination, 2026, DOI: 10.5517/ccdc.csd.cc2qfvmn; (*o*) CCDC 2515763: Experimental Crystal Structure Determination, 2026, DOI: 10.5517/ccdc.csd.cc2qfvnp; (*p*) CCDC 2515764: Experimental Crystal Structure Determination, 2026, DOI: 10.5517/ccdc.csd.cc2qfvpq; (*q*) CCDC 2515765: Experimental Crystal Structure Determination, 2026, DOI: 10.5517/ccdc.csd.cc2qfvqr.